# Searching for Free-Floating Planets with TESS: I. Discovery of a First Terrestrial-Mass Candidate

Michelle Kunimoto [1,†★], William DeRocco [2,†], Nolan Smyth [2] and Steve Bryson [3]
† Co-lead authors; these authors contributed equally to this work.
[1]Department of Physics and Kavli Institute for Astrophysics and Space Research, Massachusetts Institute of Technology, 77 Massachusetts Avenue, Cambridge, MA 02139, USA
[2]Santa Cruz Institute for Particle Physics, University of California, Santa Cruz, CA 95062, USA
[3]NASA Ames Research Center, Moffett Field, CA 94035, USA

Accepted XXX. Received YYY; in original form ZZZ



## ABSTRACT

Though free-floating planets (FFPs) that have been ejected from their natal star systems may outpopulate their bound counterparts in the terrestrial-mass range, they remain one of the least explored exoplanet demographics. Due to their negligible electromagnetic emission at all wavelengths, the only observational technique able to detect these worlds is gravitational microlensing. Microlensing by terrestrial-mass FFPs induces rare, short-duration magnifications of background stars, requiring high-cadence, wide-field surveys to detect these events. The Transiting Exoplanet Survey Satellite (TESS), though designed to detect close-bound exoplanets via the transit technique, boasts a cadence as short as 200 seconds and has monitored hundreds of millions of stars, making it well-suited to search for short-duration microlensing events as well. We have used existing data products from the TESS Quick-Look Pipeline (QLP) to perform a preliminary search for FFP microlensing candidates in 1.3 million light curves from TESS Sector 61. We find one compelling candidate associated with TIC-107150013, a source star at $d_s = 3.194$ kpc. The event has a duration $t_E = 0.074^{+0.002}_{-0.002}$ days and shows prominent finite-source features ($\rho = 4.55^{+0.08}_{-0.07}$), making it consistent with an FFP in the terrestrial-mass range. This exciting result indicates that our ongoing search through all TESS sectors has the opportunity to shed new light on this enigmatic population of worlds.

**Key words:** planets and satellites: detection – gravitational lensing: micro – planets and satellites: terrestrial planets

## 1 INTRODUCTION

Free-floating planets (FFPs), planets not bound to any star, constitute an enigmatic planetary demographic of which little is known. Theory and simulation suggest that such planets should be ubiquitous in the Galaxy (Strigari et al. 2012; Hong et al. 2018), with different formation mechanisms dominating at different FFP masses. At high masses ($\gtrsim M_{\rm Jup}$), they may form in isolation from the collapse of gas, constituting the extreme low-mass end of the stellar mass function (Padoan & Nordlund 2002; Bonnell et al. 2008; Zwart & Hochart 2024). FFPs formed through these processes may retain sufficient heat to be detected in the infrared, and recent observations have discovered an unexpectedly large abundance of such worlds (McCaughrean & Pearson 2023; Pearson & McCaughrean 2023). At terrestrial masses, however, the dominant formation mechanism is thought to be gravitational ejection from a parent system during the chaotic early phases of system formation, e.g. through planet-planet scattering (Rasio & Ford 1996; Weidenschilling & Marzari 1996; Veras & Raymond 2012), ejection by an inner binary (Nelson 2003; Sutherland & Fabrycky 2016; Smullen et al. 2016; Coleman et al. 2023; Standing et al. 2023; Chen et al. 2023; Coleman 2024), or stellar fly-bys (Wang et al. 2024; Yu & Lai 2024).

Such terrestrial-mass FFPs likely outpopulate their bound counterparts (Sumi et al. 2023a; Mroz & Poleski 2023), comprising the *majority* of Galactic exoplanets in this mass range. However, their negligible emission across the electromagnetic spectrum poses a significant observational challenge. The only technique sensitive to detecting these worlds is gravitational microlensing, in which the gravitational field of the FFP ("lens") focuses light from a distant background star ("source"), resulting in the temporary apparent magnification of the star as the lens traverses the source along the line of sight. Ground-based microlensing searches have recently yielded the first three observations of terrestrial-mass FFPs (Mróz et al. 2019; Koshimoto et al. 2023; Mróz et al. 2020). Though these observations have confirmed the existence of this population and suggested a high Galactic abundance, ground-based observations are limited by their photometric sensitivity and cadence, with atmospheric interference and technical requirements requiring magnifications of $\gtrsim 10\%$ and a cadence of $> 15$ min (e.g., Mróz et al. 2019). Typical microlensing events for terrestrial-mass FFPs have timescales on the order of an hour, and often result in magnifications well below the threshold required by ground-based efforts, making their detection extremely challenging for existing ground-based observatories.

The Transiting Exoplanet Survey Satellite (TESS; Ricker et al. 2015) has provided a relatively unexplored dataset from which new FFPs can be discovered. While TESS was optimized for detecting exoplanets via the transit method, its wide-field imaging capabilities

★ E-mail: mkuni@mit.edu

and high-cadence, high-precision photometric observations make it well-suited to also detecting short-duration microlensing events. TESS observes large $24^\circ \times 96^\circ$ sectors of the sky for 27.4 days at a time, allowing it to monitor millions of stars in its Full-Frame Images (FFIs). TESS's high photometric precision allows it to detect transit depths (and lensing peaks) as small as a fraction of a percent. Furthermore, its current 200-second FFI cadence enables sensitivity to events lasting significantly less than an hour.

In this work, we leveraged TESS's unique sensitivity to terrestrial-mass microlensing events to perform a preliminary search for FFPs within TESS Sector 61. We used a dataset consisting of 1.3 million stars with magnitudes as dim as $T = 15$ mag observed at a 200-second cadence. This initial search resulted in one potential short-duration microlensing event consistent with a terrestrial-mass FFP.

## 2 TESS SEARCH FOR FREE-FLOATING PLANETS

### 2.1 Microlensing Fundamentals

When a foreground FFP crosses near the line of sight to a background source star, its gravitational field perturbs the emitted light rays and creates multiple images of the source. When these multiple images can not be individually resolved, the net effect is an apparent time-varying magnification of the source known as gravitational microlensing. The characteristic gravitational extent of the lens, the *Einstein radius*, is given by

$$R_E = \sqrt{\frac{4GMd_l(1-d_l/d_s)}{c^2}}, \tag{1}$$

where $M$ is the mass of the lens and $d_l$ ($d_s$) is the distance to the lens (source).

The time it takes to traverse the Einstein radius is therefore

$$t_E = \frac{R_E}{v_{\rm rel}}, \tag{2}$$

where $v_{\rm rel}$ is the transverse velocity of the source-lens system relative to the observer. The net magnification of a point-source during a microlensing event can be described analytically by an overall multiplicative factor relative to its baseline flux via (Paczynski 1986)

$$A(t) = \frac{u^2+2}{u\sqrt{u^2+4}}, \tag{3}$$

where $u$ is the *impact parameter*, the displacement of the lens from the source in units of the Einstein radius. For an event centered around time $t_0$, corresponding to a minimum value of $u_0$, the impact parameter evolves as

$$u = \sqrt{\left(\frac{t-t_0}{t_E}\right)^2 + u_0^2}. \tag{4}$$

This allows one to model the magnification of the source in terms of $u_0, t_E$, and $t_0$. Along with these three parameters, two additional parameters, the baseline flux of the source ($f_s$) and blended background ($f_b$), provide a full parametrization of a point-source point-lens microlensing event.

When the angular extent of the source $\theta_s$ is comparable to or greater than the *Einstein angle* $\theta_E \equiv R_E/d_l$, the additional parameter $\rho = \theta_s/\theta_E$ describes the extent of finite-source effects in the light-curve. Finite-source effects generically reduce the peak magnification and elongate the duration of the event (see, e.g., Lee et al. (2009)), resulting in a box-like that makes the light-curve amenable to initial flagging through methods such as the Box Least Squares (BLS) search algorithm (see §3.2 and §4.2).

### 2.2 Expected Event Yield

Microlensing is an intrinsically rare phenomenon. Microlensing surveys rely upon the observation of a large number of source stars at a rapid cadence over a long observational baseline. Though TESS's transit survey was not designed with microlensing in mind, over the course of its Primary and Extended Missions, it has observed hundreds of millions of stars with continuous baselines ranging from 27.4 days to 1 year at cadences as rapid as 200 seconds. As a result, its existing observations are well-suited to a microlensing search for low-mass free-floating planets.

One can get a sense for the expected yield by performing a simple estimate of the event rate for a single source and monochromatic mass distribution of lenses. The rate can be estimated as $\Gamma \approx n v_{\rm rel} \times (u_T R_E d_s)$ (Gaudi et al. 2008), where $n$ is the number density of lenses and $u_T R_E d_s$ is the cross-sectional area spanned by the "microlensing tube" (Griest 1991), with $u_T$ defined as the threshold impact parameter required to produce a detectable magnification, and is $\approx 5$ for TESS's photometric sensitivity [1]. Using this expression, a rough estimate of the expected number of detectable low-mass FFP events in a search of existing TESS data is

$$N \approx 1 \text{ event } \left(\frac{u_T}{5}\right)\left(\frac{n}{20\ \text{pc}^{-3}}\right)\left(\frac{M}{0.1M_\oplus}\right)^{1/2} \left(\frac{v_{\rm rel}}{55\ \text{km/s}}\right)\left(\frac{d_s}{3\ \text{kpc}}\right)^{3/2}\left(\frac{N_\star}{6.67\times10^7}\right)\left(\frac{t_{\rm obs}}{27.4\ \text{days}}\right), \tag{5}$$

where the number of individual single-sector light curves $N_\star$ has been chosen to correspond to the TESS dataset of stars down to $T = 13.5$ mag for Sectors 1 - 70. We assume a typical source distance $d_s = 3$ kpc and a per-sector observational baseline $t_{\rm obs} = 27.4$ days.

The value of $n$ has been taken to coincide with the best fit of the FFP mass function suggested by the MOA collaboration (Sumi et al. 2023b) (see also Gould et al. (2022); Mroz & Poleski (2023)) and corresponds to a normalization of $\approx 22$ free-floating planets per star with masses within a half-dex of $M_\oplus$. The true abundance of FFPs in this mass range is unknown, however, and may very well be significantly higher. TESS, with its rapid cadence and high photometric sensitivity, is uniquely suited to probe this low-mass region of the mass function. The conservative estimate of Eq. (5) therefore provides considerable motivation to conduct a search for overlooked low-mass FFP microlensing events in TESS observations.

## 3 METHODOLOGY

### 3.1 Light Curves

We used FFI light curves extracted by the Quick-Look Pipeline (QLP; Huang et al. 2020), which covers all stars in the TESS Input Catalog (currently TICv8.2; Paegert et al. 2021) brighter than $T = 13.5$ mag. Since Sector 41, QLP also produces light curves for M dwarfs as faint as $T = 15$ mag (Kunimoto et al. 2022b). For TESS Sector 61 (2023 January 18 – February 12), we obtained light curves with 200-second cadence for a total of 1,286,238 targets.

[1] One can roughly estimate $u_T$ by determining the maximum impact parameter that results in an event satisfying our initial detection threshold (see §3.2), namely a magnification of $A/\sigma_{\rm phot} > 10$ for at least 5 consecutive observations averaged over TESS source stars. $\sigma_{\rm phot}$ is the median photometric noise from Kunimoto et al. (2022a) scaled to an event duration of $5 \times 30$ min, where 30 min is the cadence of the TESS Primary Mission. See DeRocco et al. (2024) for further details on estimating $u_T$.

From each light curve, we removed all data points flagged as poor quality as indicated by a quality flag of 1, as well as all data within 0.2 days of the start and end of each TESS orbit, resulting in an average observational baseline per target of 23.6 days. These times correspond to high magnification systematics caused by scattered light from the Earth or Moon. To remove low-frequency trends caused by stellar variability, we applied the biweight detrending algorithm implemented in `wotan` (Hippke et al. 2019) using a detrending window of 2 days. Given that we expect most terrestrial FFP events to have typical durations of less than one day, the 2-day window was chosen to minimize the impact of event distortion caused by detrending while removing long-term astrophysical trends.

### 3.2 Microlensing Event Detection

Transiting exoplanets are commonly found using the BLS period search algorithm (Kovács et al. 2002), which searches for periodic dimming of a target star. The shape of this signal can be approximated as a box, i.e. the dimming initiates and terminates instantaneously. BLS can also be adapted for microlensing studies by searching for *non-repeating*, *brightening* events. Though the magnification curve associated with microlensing of point-like sources is not well-approximated by a box, finite-source effects broaden this peak, resulting in light-curves that more closely resemble a box-like plateau (see §4.2 for an example displaying these effects, or Fig. 4 of Johnson et al. (2022) for further discussion). Given that the majority of our TESS targets lie within $\sim$ 3 kpc of Earth, terrestrial-mass FFPs are likely to produce events with significant finite-source effects, making the use of the BLS algorithm a reasonable initial means to flag high-SNR events of interest. BLS is also computational inexpensive, which is necessary for searching the large TESS datasets.

In particular, we used the GPU-optimized BLS algorithm implemented in `cuvarbase` (Hoffman 2022) to search each light curve. For sensitivity to FFPs across a wide range of planetary masses, we search for events with durations as short as 17 minutes (five times the 200-second FFI cadence) and as long as 1 day. We set the period of the box signal to 30 days (longer than the total length of the sector) in order to force the algorithm to search for single events.

After BLS identified the duration ($\tau$) and central time ($t_{\rm BLS}$) of a possible signal, we estimated its signal-to-noise ratio (SNR) using

$$\mathrm{SNR} = \frac{\delta}{\sigma}, \tag{6}$$

where $\delta$ is the height of the event and $\sigma$ is the noise over the event duration. This is a rough estimate of SNR that could be improved by fitting a different shape such as a trapezoid (e.g., Kipping 2023), which we will explore in future works to detect lower SNR events.

We estimated $\delta$ by finding the weighted mean of all data points over the event duration and subtracting the weighted mean of all data points at least one duration away from $t_{\rm BLS}$. We estimated $\sigma$ by taking into account correlated noise in the TESS light curves following the pink noise definition from Pont et al. (2006) as

$$\sigma = \sqrt{\frac{\sigma_w^2}{n} + \sigma_r^2}, \tag{7}$$

where $\sigma_w$ is the white noise in the light curve, $\sigma_r$ is the red noise, and $n$ is the number of in-event data points. We take $\sigma_w$ to be equal to the weighted standard deviation of the light curve after masking out data within one event duration of $t_{\rm BLS}$. Following Hartman & Bakos (2016), we estimate $\sigma_r$ using the expression

$$\sigma_r^2 = \sigma_{\rm bin}^2 - \sigma_{\rm bin,thy}^2, \tag{8}$$

where $\sigma_{\rm bin}$ is the weighted standard deviation of the residual light curve after binning in time with a bin-size equal to the duration of the transit, and $\sigma_{\rm bin,thy}$ is the expected standard deviation of the binned light curve if the noise were uncorrelated in time. If $\sigma_r$ is estimated to be less than zero, we set $\sigma_r = 0$.

In order for a signal to be considered an initial candidate to be vetted further, we required SNR $> 10$ and $n \geq 5$.

### 3.3 Automated Flux-Level Vetting

A total of 58,303 signals met our basic detection criteria and were sent through a first round of automated vetting, which involved computing a set of metrics to be compared to pass-fail thresholds. If a signal failed to meet any of our criteria, it was rejected as a possible microlensing candidate. We do not claim that these empirically-determined thresholds are optimal and, as is the case for any vetting procedure, they may have removed true signals as well as false positives. However, they successfully produced a dataset of microlensing candidates amenable to manual inspection (§3.5).

#### *3.3.1 Initial Model Fitting*

Each signal was first fit to three different models: a straight line parameterized by a slope and offset; a skew normal distribution parameterized by a central timescale, amplitude, scale ($\omega$), and shape ($\alpha$); and a simple point-source lens model parameterized by $t_0$, $u_0$, and $t_E$. Fitting was performed using the `lmfit` Python package (Newville et al. 2016). Data more than $2\tau$ from $t_{\rm BLS}$ were ignored in order to speed up the fitting process.

A candidate was rejected if a point lens was a worse fit compared to a straight line according to the reduced $\chi^2$ of each fit, i.e., $\chi^2_{\rm lens} > \chi^2_{\rm line}$. Only 526 signals failed this criteria; however, the fit results were more useful for other tests targeted at specific types of false positives.

#### *3.3.2 Edge Effects and Gapped Events*

BLS occasionally triggers at the edge of data gaps, especially if such edges correspond to rapid increases in brightness due to scattered light, a well-known systematic effect within TESS data. A number of events also lack a significant amount of data either during the brightening, or just before and/or after. To identify these cases, we computed the fraction of the light curve near the event that actually contained data. We found $n_{\rm exp}$, the number of data points expected within $2\tau$ of $t_{\rm BLS}$ given the 200-second cadence of the observations, as well as $n_{\rm obs}$, the number of data points actually observed over that time. We rejected 46,117 signals with $n_{\rm obs}/n_{\rm exp} < 0.9$. Given that this cut rejected 79% of all vetted signals, edge effects and gapped events constituted the majority of TESS microlensing false positives.

#### *3.3.3 Non-Unique Events*

Microlensing events are rare, and should therefore be unique compared to other events in the light curve with the same duration. The presence of similar features at other times in a light curve suggest short-term periodic or quasi-periodic stellar variability, or low-SNR noise/instrumental systematics. To quantify uniqueness, we adopted elements from the Model-Shift Uniqueness Test developed for Kepler

transiting exoplanet candidate vetting (Coughlin 2017). In summary, we computed an SNR time series by finding the SNR of events centered at each point in the light curve over the duration of the BLS-detected signal. We measured the significance of the primary microlensing event ($SNR_{pri}$) as the largest SNR value in the SNR time series within a half event duration of the BLS detection. The most significant event at least two event durations from the primary was labeled the secondary event ($SNR_{sec}$), and the next most significant event at least two event durations from both the primary and secondary was labeled the tertiary event ($SNR_{ter}$). Finally, the most significant negative event ($SNR_{neg}$), representing the largest flux decrease at least three event durations from the primary and secondary, was also labeled.

We rejected signals for which the primary event was not sufficiently unique, as quantified by $SNR_{pri} < 10$ or $\Delta SNR < 2$ compared to all other events (the secondary, tertiary, or most negative events). A total of 6,797 signals failed this criteria.

#### *3.3.4 Flares*

Flares are highly asymmetric brightening events characterized by a rapid increase in flux followed by a gradual decay, in contrast to the symmetric, bell-shaped peaks of microlensing events. We used the results of the skew normal distribution fit to identify this class of false positives. We rejected 41,615 signals with a skew shape of $|\alpha| > 2$, suggesting strong asymmetry. Half of these also failed the edge effect/gapped event test, indicating that they were likely asymmetric events caused by scattered light. We also rejected 2,152 signals with a skew scale of $\omega < 0.01$ days, as these are consistent with extremely short-duration flares or single-cadence events such as cosmic ray hits.

### 3.4 Asteroid Rejection

A total of 6,524 signals passed all previous tests, and the most common remaining false positive scenario was brightening events caused by passing asteroids. We employed three major tests to reject asteroids: *(1)* cross-matching our candidates with known objects in the Solar System, *(2)* analyzing each event at the pixel level, and *(3)* searching for indications of moving bodies by matching correlated events across RA and Dec space.

*(1) Known asteroids:* We queried the NASA/JPL Small-Body Identification API[2] for all known small bodies seen by TESS within the entire region in RA and Dec covered by Sector 61 in each camera and CCD combination, extracting all objects brighter than 21 mag seen between 2962.79 and 2990.29 TESS BJD in steps of 2.5 days. We found 8,270 unique objects. Ephemerides for each were generated in 30-minute intervals using the JPL Horizons Solar System data and ephemeris computation service[3]. We then calculated the angular separation and difference in time between each asteroid and each surviving signal. We rejected 6,124 signals with angular separation of $< 0.07°$ and time difference of $< 0.2$ days.

*(2) Pixel-level analysis:* Hundreds of asteroids were not rejected by this automated cut due to incompleteness of the Small-Body Database. We further removed asteroids by inspecting each candidate at the pixel level. Using $21 \times 21$ pixel cutouts centered on each target star produced by `tesscut` (Brasseur et al. 2019), we computed the mean of all out-of-event images to represent the typical field near a source star when no brightening or dimming events are occurring on average. Out-of-event times were defined as those between $0.5\tau$ and $1.5\tau$ from the center of each event. We then subtracted the mean out-of-event image from each individual image in order to find the pixels undergoing the largest brightening at each point in time. We searched for changes in the locations of the brightest pixels within $1.5\tau$ of the event, which are consistent with an asteroid moving across the TESS pixels. Examples showing the maximum values of each pixel, for both an asteroid and a likely isolated candidate, are provided in Figure 1, highlighting the clear difference between the two scenarios.

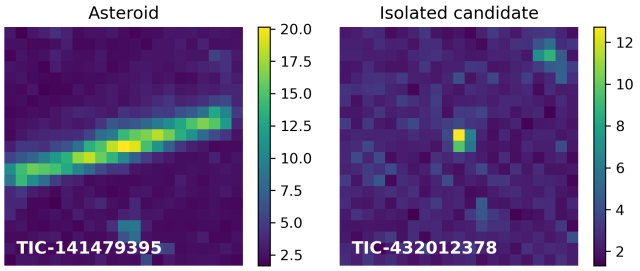


**Figure 1.** Pixel-level data demonstrating typical signatures for asteroids (left) compared to isolated events (right), using examples associated with TIC-141479395 and TIC-432012378, respectively. These data were produced by subtracting the mean out-of-event image from each image within $1.5\tau$ of the center of a given candidate event, and finding the maximum value of each pixel.

We also produced difference images, employing the same techniques commonly used for transiting exoplanet vetting (Bryson et al. 2013), with the TESS difference imaging codebase `transit-diffImage`.[4] Difference images are used to confirm that an event is co-located with the target star, rather than being due to a nearby contaminant. Moving objects appear smeared out in difference images, while on-target microlensing events remain isolated.

*(3) RA/Dec event correlation:* As a final check, we inspected the RA-Dec distribution of our candidates to search for extended trails as the objects move across the TESS field and cause brightening events on different stars. We identified multiple trails, all of which also corresponded to asteroids identified through our pixel-level analysis. Between our pixel-level and RA-Dec investigations, we rejected another 278 signals as likely asteroids.

Note that we initially implemented the single-linkage clustering algorithm described by McDonald et al. (2021) to automatically flag these correlated structures. However, we found that the low relative stellar density of the TESS field of view with respect to K2 limited the efficacy of this method, and we removed it from our vetting procedure. In future work to further automate the process, we plan to instead incorporate shift-and-stack methods (e.g., Holman et al. 2019; Payne et al. 2019), which have already been used to detect asteroids with TESS FFI data (Woods et al. 2021).

### 3.5 Manual Inspection

We manually inspected both light curves and difference images for the surviving 122 candidates in order to confirm that the events appeared symmetric, unique, and consistent with our expectations for on-target lensing events. Most events that quickly failed visual inspection were

[2] https://ssd-api.jpl.nasa.gov/doc/sb_ident.html
[3] https://ssd.jpl.nasa.gov/horizons/
[4] https://github.com/stevepur/transit-diffImage

obvious detrending artifacts caused by discontinuities in the QLP light curves, or were caused by stellar variability that fell beyond the thresholds of the cuts used during the automated vetting procedure. In some cases, inspection of the difference images revealed that a lensing candidate was offset from its true source. Such events were further investigated using the light curve of the correct source; all turned out to be variable stars.

Based on flux- and pixel-level data from Sector 61 alone, we found two high-SNR signals associated with TIC-123147666 and TIC-107150013 that appeared to be possible microlensing signals. However, a single TESS sector is insufficient for identifying repeating events that occur on timescales near or longer than 27 days, such as periodic brightening events caused by tidal distortion in highly eccentric binary star systems (e.g., KOI-54; Welsh et al. 2011).

We visually inspected all available TESS observations for our most promising candidates in search of repeated events, and found that TIC-123147666 featured similar brightening events in all other TESS sectors (Sectors 7, 8, 34, 35, and 62), consistent with a period of 26.2 days. This star was also previously identified as having a proper motion anomaly between the long-term proper motion vector and Gaia DR2 and HIPPARCOS measurements, indicative of the presence of a perturbing secondary object (Kervella et al. 2019). TIC-123147666 also has a high Renormalized Unit Weight Error (RUWE) value (8.10) according to Gaia DR3 observations (Gaia Collaboration et al. 2016, 2021), consistent with having a companion (Lindegren et al. 2018, 2021). We therefore classify TIC-123147666 as a false positive likely due to tidal interactions with a binary companion. Upon revisiting several of our other high-SNR, non-asteroid signals that had been manually rejected due to lack of consistency with lens models, we found that many were associated with repeating events throughout other TESS sectors. Future vetting efforts could be substantially improved and further automated by incorporating multi-sector data earlier in the process.

In contrast to TIC-123147666, we found no repeating events in other sectors for TIC-107150013 (Sectors 7 and 34), and the pre-detrended light curves had no indications of significant stellar variability or flares (Figure 2). Furthermore, its low RUWE value (0.99) is consistent with a single star, disfavoring the presence of an unresolved binary companion associated with this source.

It remains possible that a periodic signal may have fallen within the large data gaps between Sectors 7, 34, and 61; the planned 54 days of continuous observations of this star across TESS sectors 87 and 88 (2024 December 18 – 2025 February 11) will provide a future opportunity to rule out long-period signals. However, given the multiple lines of evidence that this star is not influenced by a binary companion, we take TIC-107150013 to be solitary and proceed with it as the source associated with our one remaining candidate lensing event.

## 4 RESULTS AND DISCUSSION

TIC-107150013 is located at a distance from Earth of $d_s = 3193 \pm 153$ pc based on parallax from Gaia DR3 (Table 1). Lacking a stellar radius from Gaia DR3, we adopt $R_s = 12.91^{+0.96}_{-1.51}\ R_\odot$ from Gaia DR2 (Gaia Collaboration et al. 2016, 2018). The star lies only 5.03° below the Galactic equator, making it a relatively crowded region of the sky; however, at $T = 13.10$ mag, TIC-107150013 is the brightest star within 1′. The microlensing candidate event occurs at $t_{\rm BLS} = 2987.03$ days, was detected by BLS with a duration of $\tau = 0.38$ days, and has a high SNR of 31 (Figure 3). In order to further assess the event's candidacy, we analyzed the same signal using multiple light-curve extraction methods and sperformed dedicated lens modeling including second-order effects arising from the non-negligible angular extent of the source and limb-darkening.

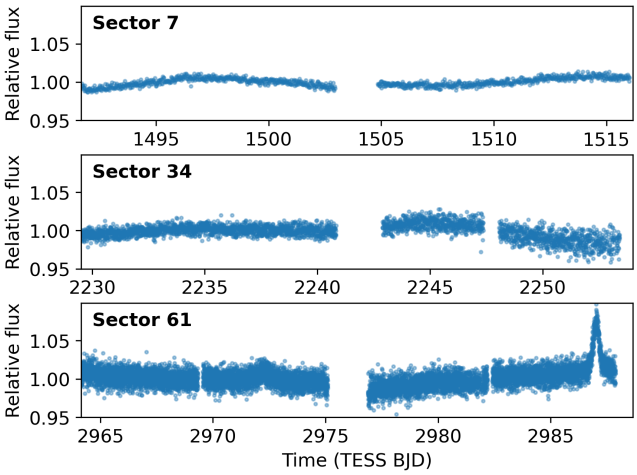


**Figure 2.** Pre-detrended QLP light curves from Sectors 7, 34, and 61 for TIC-107150013, demonstrating that the microlensing candidate at 2987 days is a single, unique event based on the available TESS observations.

### 4.1 Alternative Light Curve Extraction

QLP produces light curves using an aperture photometry approach combined with difference imaging. A reference image is constructed using the median combination of good quality images and this reference is subtracted from each frame to produce difference images. Aperture photometry is performed on the difference images to produce a difference flux time series, and the TESS magnitude provided in the TIC is used to scale the difference fluxes relative to the star's average flux. The end result is a de-blended flux time series assuming any variations observed are associated with the target star (Huang et al. 2020). This approach relies on an accurate estimate of the star's TESS magnitude, and the amplitude of the microlensing event will be inaccurate if the target star is not the true source.

To test the sensitivity of the interpretation of our candidate to an alternative method, we extracted a new Sector 61 light curve using the TESS-Gaia Light Curve (TGLC) procedure (Han & Brandt 2023) with a $50 \times 50$ pixel FFI cutout size. TGLC produces both aperture and point spread function (PSF) high-precision light curves corrected for contamination from nearby stars based on star positions and magnitudes from Gaia DR3. Here we adopt the TGLC aperture light curves, which offer more reliable amplitude estimates for dim stars in crowded fields like TIC-107150013 (Han & Brandt 2023). The TGLC aperture light curves are produced by performing aperture photometry on a $3 \times 3$ pixel aperture centred on the target star. To correct for contamination, TGLC estimates the median total flux of nearby stars in the Gaia DR3 catalog as well as the percentage of the target star's light that falls on the aperture based on the shape of an effective PSF model. The aperture light curve's median is shifted to the Gaia-predicted median multiplied by this percentage, resulting in a de-blended light curve corrected for the contamination of all known stars resolved by Gaia DR3.

Because our original detrending process can be destructive to the shapes of high-SNR lensing events, we also re-detrended each light curve while masking out data within $0.5\tau$ of the event to minimize

**Table 1.** Stellar Parameters for TIC-107150013

| Parameter | Value | Description | Source |
|---|---|---|---|
| | | *TIC Parameters* | |
| ID | 107150013 | TESS Input Catalog ID | TICv8.2 |
| $T_{\rm eff}$ | $4115 \pm 123$ | Effective temperature (K) | TICv8.2 |
| $R_s$ | $12.91^{+0.96}_{-1.51}$ | Stellar radius ($R_\odot$) | Gaia DR2 |
| | | *Astrometric Parameters* | |
| RA | 07:22:30.806 | Right ascension (J2016) | Gaia DR3 |
| Dec | -25:29:15.77 | Declination (J2016) | Gaia DR3 |
| $\bar{\omega}$ | $0.313 \pm 0.015$ | Parallax (mas) | Gaia DR3 |
| $\mu_\alpha$ | $-0.395 \pm 0.010$ | Proper motion right ascension (mas yr$^{-1}$) | Gaia DR3 |
| $\mu_\delta$ | $0.260 \pm 0.016$ | Proper motion declination (mas yr$^{-1}$) | Gaia DR3 |
| | | *Photometric Parameters* | |
| $T$ | $13.0985 \pm 0.0071$ | TESS band magnitude (mag) | TICv8.2 |
| $B$ | $17.228 \pm 0.162$ | $B$ band magnitude (mag) | UCAC4 (Zacharias et al. 2013) |
| $V$ | $14.922 \pm 0.103$ | $V$ band magnitude (mag) | UCAC4 |
| $G$ | $14.017 \pm 0.002$ | Gaia $G$ band magnitude (mag) | Gaia DR3 |
| $J$ | $11.63 \pm 0.026$ | $J$ band magnitude (mag) | 2MASS (Skrutskie et al. 2006) |
| $H$ | $10.91 \pm 0.022$ | $H$ band magnitude (mag) | 2MASS |
| $K_s$ | $10.64 \pm 0.023$ | $K$ band magnitude (mag) | 2MASS |
| $W1$ | $10.453 \pm 0.022$ | $W1$ band magnitude (mag) | WISE (Wright et al. 2010) |
| $W2$ | $10.538 \pm 0.020$ | $W2$ band magnitude (mag) | WISE |
| $W3$ | $10.373 \pm 0.075$ | $W3$ band magnitude (mag) | WISE |

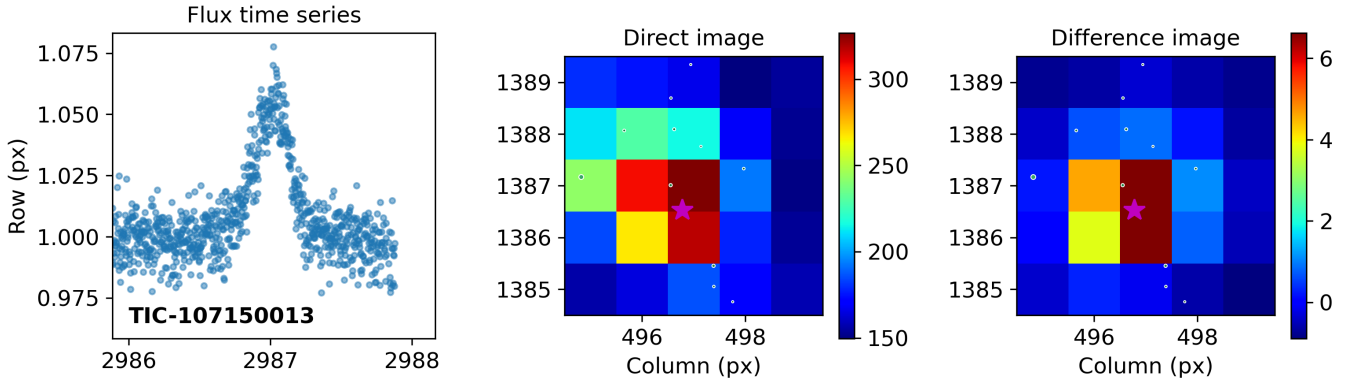


**Figure 3.** Flux- and pixel-level data associated with the source star TIC-107150013, which features a high-SNR (SNR = 31) microlensing candidate event at 2987 days. The direct image reflects the typical field near the target (pink star), while the difference image reflects the pixels undergoing the largest brightening over the event. White circles show the locations of all stars down to 4 magnitudes fainter than the target star, with sizes scaled by brightness. The difference image is consistent with the lensing candidate being co-located with the target star.

distortion of the microlensing signal. The re-detrended QLP and TGLC light curves are shown in Figure 4, with the signal at 2987 days clearly visible in both datasets. Because the TGLC light curve has better precision, with an out-of-event flux standard deviation of 6448 ppm compared to 8603 ppm in the QLP light curve, we adopt the TGLC light curve for our preferred results in further analysis.

### 4.2 Lens Modeling

We fit both QLP and TGLC light curves using point-source point-lens (PSPL) and finite-source point-lens (FSPL) models with linear limb-darkening, as implemented by the `pyLIMA` lensing model package (Bachelet et al. 2017). For the FSPL fits we used the `pyLIMA` `FSPLargemodel`, which is appropriate for the finite source magnification of large stars. We adopted a linear limb-darkening coefficient of 0.68 based on TESS values estimated by Claret (2017) for relatively cool giant stars ($\log g \sim 2.5$, $T_{\rm eff} \sim 4100$ K). We fixed the blending fraction to zero given that: (a) the light curves produced by the TGLC and QLP extractions have already undergone de-blending of resolved stars (§4.1), and (b) the nominal source is very bright in comparison to unresolved background stars, dominating the flux. Parallax effects due to the motion of the satellite are negligible on these timescales for all realistic lens masses and distances,[5] and thus were

[5] One can estimate the order of magnitude of this effect by taking TESS's displacement during the event to be $\Delta d \sim 25,000$ km and estimating $\pi_E \approx$

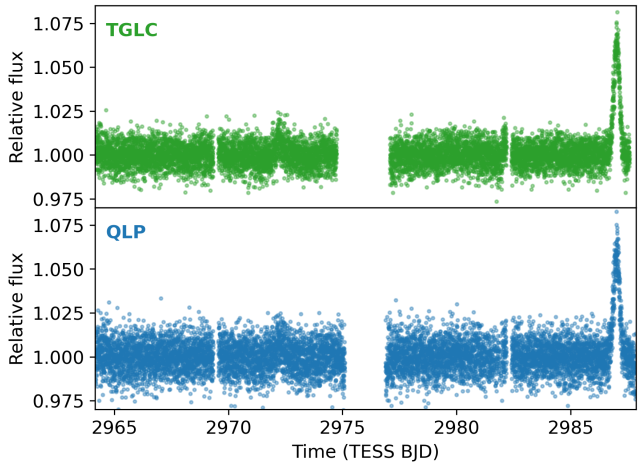


**Figure 4.** Detrended Sector 61 light curves for TIC-107150013, as extracted by TGLC (top) and QLP (bottom). The microlensing candidate at 2987 days is visually consistent between the two light curves, with similar shape, duration, and amplitude.

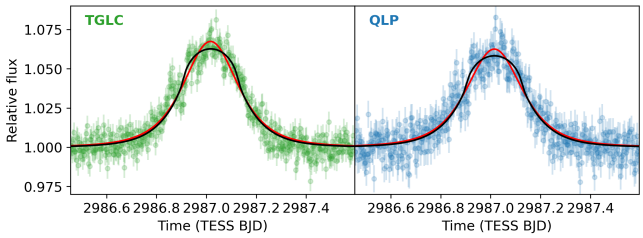


**Figure 5.** The TESS microlensing candidate associated with the source star TIC-107150013, as seen in TGLC (left) and QLP (right) sector 61 light curves. The red lines show the median PSPL fits, while the black lines show the median FSPL model fits. Based on comparing log $Z$ values for each result, the FSPL fits are overwhelmingly preferred.

not included in the fit. Ultimately, we performed three-parameter PSPL fits parameterized by $t_0$, $u_0$, and $t_E$, and four-parameter FSPL fits with the additional parameter $\rho$.

To explore the parameter space, we used the `multinest` Bayesian inference tool (Feroz et al. 2009) with 500 live points. We removed all data more than 2 days from $t_{\rm BLS}$ to speed up the fit. The TGLC and QLP fits converged after $\lesssim 25,000$ total likelihood computations, giving the results shown in Table 2 and Figure 5. `multinest` also provides the Bayesian log-evidence (log $Z$) for each model, which can be used for model selection. The PSPL fits had significantly smaller log $Z$ values compared to the FSPL fits ($\log Z_{\rm FSPL} - \log Z_{\rm PSPL} = 12.0 \pm 0.3$ and $7.8 \pm 0.3$ for TGLC and QLP, respectively), indicating that the FSPL fits are overwhelmingly preferred. The TGLC corner plots for the FSPL fit are shown in Figure 6.

The peak amplitude in the QLP light curve appears to be $\sim 0.4\%$ shallower than in the TGLC light curve, likely due to the more accurate dilution estimates in TGLC light curves compared to those of QLP. Consequently, we find FSPL $u_0$ and $\rho$ values that differ at the $2\sigma$ and $1.5\sigma$ level, respectively. However, both fits detect

$\Delta d/R_E$. This is $\lesssim 0.15$ for $M \sim 0.1 M_\oplus$ and $d_l \sim 0.5$ kpc and only decreases with increasing mass and lens distance.

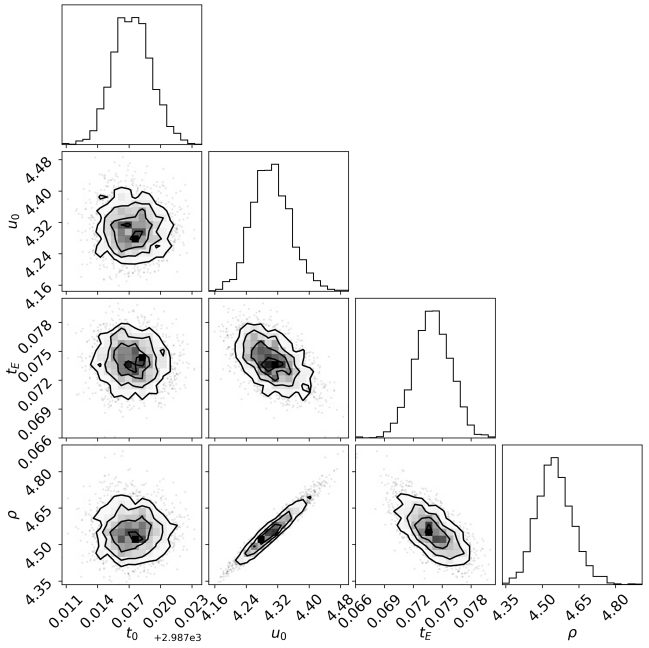


**Figure 6.** Corner plot displaying the `multinest` posteriors from the FSPL fit to the TGLC light curve of TIC-107150013.

significant and similar finite-source effects, with the TGLC fit finding $\rho = 4.55^{+0.08}_{-0.07}$ and the QLP fit finding $\rho = 4.73^{+0.12}_{-0.09}$. We take the discrepancy in these two results as an indicator of systematic uncertainty associated with our extraction methodology.

### 4.3 Lens Mass and Velocity Constraints

The appearance of finite-source features in the light curve allows us to directly estimate the Einstein angle of the lens, which in turn provides constraints on the lens mass and relative velocity. Given TIC-107150013's distance of $d_s = 3193 \pm 153$ pc and radius of $R_s = 12.91^{+0.96}_{-1.51}\ R_\odot$, its angular size is $\theta_s = 9.11^{+0.81}_{-1.15} \times 10^{-11}$ radians. Assuming $\rho = 4.55^{+0.08}_{-0.07}$ from the TGLC fit, this corresponds to an Einstein angle of $\theta_E = 2.0^{+0.2}_{-0.3} \times 10^{-11}$ radians, or $4.1^{+0.4}_{-0.5}$ $\mu$as. Solving Eq. (1) for the mass of the lens at a given lens distance, we found that our lens candidate is consistent with a planetary-mass object (Figure 7, blue curve). Similarly, $v_{\rm rel}$ can be estimated from Eq. (2), which for $t_E = 0.074$ days yields values on the order of 100 km/s (Figure 7, red curve). In Fig. 7, the shaded regions correspond to the uncertainty associated with measured values of $R_s$ and $d_s$ (Table 1). The formal uncertainties in the fit parameters for $\rho$ induce negligible changes to the lens mass and relative velocity estimates. Adopting instead the QLP value $\rho = 4.73$ results in a uniform $\approx 7\%$ reduction in the mass estimates.

Though the nature of the lens cannot be directly measured through microlensing alone, these estimates provide strong motivation that the short-duration event associated with TIC-107150013 was due to a planetary-mass object moving at a velocity consistent with typical Galactic velocities, and we therefore label this event the first FFP candidate detected by TESS.

**Table 2.** Best-fit PSPL and FSPL model parameters based on the TGLC and QLP Sector 61 light curves of TIC-107150013. The central values are the median of the posteriors, with lower and upper uncertainties from the 16th and 84th percentiles. We also report the Bayesian log-evidence values for each model, computed with `multinest`, indicating that the FSPL fits are preferred.

| Parameter | Prior | TGLC Fit (PSPL) | QLP Fit (PSPL) | TGLC Fit (FSPL) | QLP Fit (FSPL) |
|---|---|---|---|---|---|
| $t_0$ | $\mathcal{U}(2986.6, 2987.4)$ | $2987.017^{+0.002}_{-0.002}$ | $2987.015^{+0.003}_{-0.003}$ | $2987.017^{+0.002}_{-0.002}$ | $2987.015^{+0.003}_{-0.003}$ |
| $u_0$ | $\mathcal{U}(0, 10)$ | $1.929^{+0.010}_{-0.009}$ | $1.979^{+0.013}_{-0.012}$ | $4.30^{+0.05}_{-0.05}$ | $4.48^{+0.08}_{-0.07}$ |
| $t_E$ | $\mathcal{U}(0.01, 1)$ | $0.088^{+0.001}_{-0.001}$ | $0.088^{+0.002}_{-0.002}$ | $0.074^{+0.002}_{-0.002}$ | $0.074^{+0.002}_{-0.002}$ |
| $\rho$ | $\mathcal{U}(5\times10^{-5}, 100)$ | - | - | $4.55^{+0.08}_{-0.07}$ | $4.73^{+0.12}_{-0.09}$ |
| $\log Z$ | | $-554.2 \pm 0.2$ | $-596.5 \pm 0.2$ | $-542.1 \pm 0.2$ | $-588.6 \pm 0.2$ |

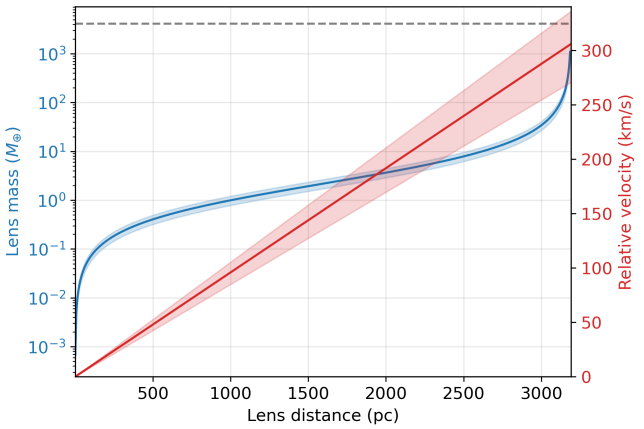


**Figure 7.** Lens masses (blue) and relative velocities (red) at different lens distances based on the FSPL fits to the TGLC light curve. The shaded regions correspond to the 16th to 84th percentiles of the fit results, with uncertainties from $R_s$ and $d_s$ propagated, while the solid line corresponds to the median values. The dotted grey line corresponds to 13 $M_{\rm Jup}$, which we assume is the largest possible planetary mass. At all lens distances, our candidate is consistent with a planetary mass object moving at typical Galactic velocities.

### 4.4 Consistency with Expected Yield

Due to the expected increased abundance of FFPs with decreasing mass (Sumi et al. 2023b; Gould et al. 2022; Mroz & Poleski 2023), events observed by TESS are expected to be largely due to FFPs with masses on the order of $10^{-2} - 10^{-1}\ M_\oplus$, below which the typical FFP would not produce a detectable magnification given TESS's sensitivity. As such, it is surprising to find an event consistent with a lens mass of $1-10\ M_\oplus$ in a search of a single sector. Rescaling Eq. (5) to $M = M_\oplus$, $N_\star = 1.3\times10^6$, $n = 2.2\ \mathrm{pc}^{-3}$ (the best-fit value of Sumi et al. (2023b)), and $t_{\rm obs} = 23.6$ days (the average duration of Sector 61 observations after removal of poor quality data, and additional gap and edge cuts, §3.1), we find that the odds of detecting such an event are on the order of 1 in 100.

One possible explanation for our discovery, in light of low expected yields, is that we were simply lucky to have observed this candidate in our first TESS sector. Further searches of the TESS dataset may not uncover new candidates at the same rate of one event per sector. To test this assumption, we performed a preliminary search of an additional 6,213,765 QLP light curves across Sectors 62 – 65 following the same light curve processing, lensing search, and automated vetting procedure described here for Sector 61. While we have not yet manually reviewed or modeled all results to the same level of detail, we did not identify any new candidates similar to TIC-107150013. All similarly high-SNR candidates detected in these sectors were removed by the vetting procedure as asteroids or false positives with shapes inconsistent with a lens model. The only potential candidates remaining (to be explored in future works) possess significantly lower SNR than the event in Sector 61, and the signatures of a microlensing signal are not immediately apparent. If we revise our expected yield estimates from Eq. (5) with this larger dataset, we find that the probability of finding a terrestrial-mass lensing event within the data becomes approximately 1 in 20.

An alternative, more tantalizing explanation is that low-mass FFPs may be *significantly* more abundant than we expect. Given that TESS is uniquely suited to detecting a large number of terrestial-mass FFPs, we may only now be tapping into an enormous population of low-mass rogue worlds. Future searches of the TESS dataset will be crucial for better understanding the abundance and demographics of FFPs. Additionally, a more speculative explanation is that there exists a different population of dark lenses in this mass range, as has been suggested by previous studies of ground-based microlensing events (Mróz et al. 2017; Niikura et al. 2019). In particular, a macroscopic subcomponent of dark matter, such as primordial black holes (PBHs; see e.g. Carr & Kühnel (2022) for a review), fits our observation well. The high relative velocity we measure aligns with the expectation for a virialized halo of dark matter; furthermore, the detection of a single event in Sector 61 matches the abundance of the putative population of PBHs suggested by Niikura et al. (2019).[6] If such a population of PBHs truly does exist, our ongoing search of other TESS sectors will provide key insight into its abundance and distribution.

## 5 SUMMARY AND FUTURE DIRECTIONS

We have announced the detection of the first free-floating planet candidate found with TESS data. Identified in a search of Sector 61 FFI light curves for short-duration microlensing events, the event is associated with TIC-107150013, a source sitting at $d_s = 3.193$ kpc with radius $R_s = 12.9\ R_\odot$. Fitting the observed signal with a four-parameter finite-source lensing model yields an Einstein-crossing time of $t_E = 0.074^{+0.002}_{-0.002}$ days and finite-source parameter $\rho = 4.55^{+0.08}_{-0.07}$, implying an Einstein radius of $\theta_E = 4.1^{+0.4}_{-0.5}\ \mu$as. This value places the lens firmly in the terrestrial-mass range, with a mass less than 10 $M_\oplus$ if within $\sim$ 2.6 kpc, and less than 1 $M_\oplus$ if within $\sim$ 1 kpc.

This initial result demonstrates that TESS has the opportunity to significantly improve our understanding of FFPs with terrestrial and sub-terrestrial masses, a range of the FFP mass spectrum that is

[6] For example, taking values within the parameter space suggested by Niikura et al. (2019) of $M = 5\ M_\oplus$, $v_{\rm rel} \approx 270$ km/s, and fraction of dark matter in PBHs $f_{\rm PBH} = 5\times10^{-2}$, rescaling Eq. (5) yields an expected number of events in Sector 61 of $\approx 1$.

poorly-constrained and will remain challenging to observe even in future surveys, such as the Roman Space Telescope's Galactic Time Domain Survey (GBTDS) (Gaudi 2022). Furthermore, the search presented here is preliminary, having been based on a small and relatively bright subset of all TESS target stars. We are currently repeating our search across all TESS sectors, and plan to use a fainter dataset of TGLC light curves down to $T = 16$ mag. This combination will increase the number of possible source stars by over two orders of magnitude. These data will allow us to confirm the existence of the population suggested by the observed FFP candidate in Sector 61, as well as to characterize its origin. The results of these ongoing searches will help inform theoretical studies of formation mechanisms for rogue planets, and will play a crucial role in calibrating the expected yield and search strategy of the GBTDS. Though never intended as a microlensing satellite, TESS is opening a window to the dark, enigmatic population of worlds that lie drifting between the stars.

## ACKNOWLEDGEMENTS

We thank Te Han for discussions about TGLC light curves, and Avi Shporer for discussions about follow-up prospects for our evolving candidates. MK acknowledges support by the Juan Carlos Torres postdoctoral fellowship from the MIT Kavli Institute for Astrophysics and Space Research. WD and NS acknowledge the support of DOE grant No. DE-SC0010107.

This paper includes data collected by the TESS mission, which are publicly available from the Mikulski Archive for Space Telescopes (MAST). Funding for the TESS mission is provided by NASA's Science Mission directorate. We acknowledge the use of public TESS data from pipelines at the TESS Science Office and at the TESS Science Processing Operations Center. This work has made use of data from the European Space Agency (ESA) mission *Gaia* (https://www.cosmos.esa.int/gaia), processed by the *Gaia* Data Processing and Analysis Consortium (DPAC, https://www.cosmos.esa.int/web/gaia/dpac/consortium). Funding for the DPAC has been provided by national institutions, in particular the institutions participating in the *Gaia* Multilateral Agreement.

## DATA AVAILABILITY

All 1.3 million QLP light curves from Sector 61 (and additional QLP light curves used for this work, including the 6.2 million light curves from Sectors 62 – 65) are publicly available as High-Level Science Products (HLSPs) on MAST at https://archive.stsci.edu/hlsp/qlp. Our additional TGLC light curve for TIC-107150013 was extracted using TGLC version 0.6.0, following the tutorial detailed at https://github.com/TeHanHunter/TESS_Gaia_Light_Curve. We set the target ID to TIC 107150013, FFI cut-out size to 50, and sector number to 61.

## REFERENCES

Bachelet E., Norbury M., Bozza V., Street R., 2017, AJ, 154, 203
Bonnell I. A., Clark P., Bate M. R., 2008, Monthly Notices of the Royal Astronomical Society, 389, 1556–1562
Brasseur C. E., Phillip C., Fleming S. W., Mullally S. E., White R. L., 2019, Astrocut: Tools for creating cutouts of TESS images, Astrophysics Source Code Library, record ascl:1905.007
Bryson S. T., et al., 2013, PASP, 125, 889
Carr B., Kühnel F., 2022, SciPost Physics Lecture Notes
Chen C., Martin R. G., Lubow S. H., Nixon C. J., 2023, Tilted circumbinary planetary systems as efficient progenitors of free-floating planets (arXiv:2310.15603)
Claret A., 2017, A&A, 600, A30
Coleman G. A. L., 2024, On the properties of free floating planets originating in circumbinary planetary systems (arXiv:2403.18481)
Coleman G. A. L., Nelson R. P., Triaud A. H. M. J., Standing M. R., 2023, Constraining the formation history of the TOI-1338/BEBOP-1 circumbinary planetary system (arXiv:2310.11898)
Coughlin J. L., 2017, Description of the TCERT Vetting Reports for Data Release 25, Kepler Science Document KSCI-19105-002
DeRocco W., Frangipane E., Hamer N., Profumo S., Smyth N., 2024, Physical Review D, 109
Feroz F., Hobson M. P., Bridges M., 2009, MNRAS, 398, 1601
Gaia Collaboration et al., 2016, A&A, 595, A1
Gaia Collaboration et al., 2018, A&A, 616, A1
Gaia Collaboration et al., 2021, A&A, 649, A1
Gaudi B. S., 2022, in Bulletin of the American Astronomical Society. p. 102.146
Gaudi B. S., et al., 2008, ApJ, 677, 1268
Gould A., et al., 2022, Journal of The Korean Astronomical Society, 55, 173
Griest K., 1991, ApJ, 366, 412
Han T., Brandt T. D., 2023, AJ, 165, 71
Hartman J. D., Bakos G. Á., 2016, Astronomy and Computing, 17, 1
Hippke M., David T. J., Mulders G. D., Heller R., 2019, AJ, 158, 143
Hoffman J., 2022, cuvarbase: fast period finding utilities for GPUs, Astrophysics Source Code Library, record ascl:2210.030
Holman M. J., Payne M. J., Pál A., 2019, Research Notes of the American Astronomical Society, 3, 160
Hong Y.-C., Raymond S. N., Nicholson P. D., Lunine J. I., 2018, ApJ, 852, 85
Huang C. X., et al., 2020, Research Notes of the American Astronomical Society, 4, 204
Johnson S. A., Penny M. T., Gaudi B. S., 2022, The Astrophysical Journal, 927, 63
Kervella P., Arenou F., Mignard F., Thévenin F., 2019, A&A, 623, A72
Kipping D., 2023, MNRAS, 523, 1182
Koshimoto N., et al., 2023, Terrestrial and Neptune mass free-floating planet candidates from the MOA-II 9-year Galactic Bulge survey (arXiv:2303.08279)
Kovács G., Zucker S., Mazeh T., 2002, A&A, 391, 369
Kunimoto M., Winn J., Ricker G. R., Vanderspek R. K., 2022b, AJ, 163, 290
Kunimoto M., Winn J., Ricker G. R., Vanderspek R. K., 2022a, The Astronomical Journal, 163, 290
Lee C. H., Riffeser A., Seitz S., Bender R., 2009, ApJ, 695, 200
Lindegren L., et al., 2018, A&A, 616, A2
Lindegren L., et al., 2021, A&A, 649, A2
McCaughrean M. J., Pearson S. G., 2023, arXiv e-prints, p. arXiv:2310.03552
McDonald I., et al., 2021, MNRAS, 505, 5584
Mroz P., Poleski R., 2023, Exoplanet Occurrence Rates from Microlensing Surveys (arXiv:2310.07502)
Mróz P., et al., 2017, Nature, 548, 183
Mróz P., et al., 2019, Astronomy & Astrophysics, 622, A201
Mróz P., et al., 2020, The Astrophysical Journal Letters, 903, L11
Nelson R. P., 2003, MNRAS, 345, 233
Newville M., Stensitzki T., Allen D. B., Rawlik M., Ingargiola A., Nelson A., 2016, Lmfit: Non-Linear Least-Square Minimization and Curve-Fitting for Python, Astrophysics Source Code Library, record ascl:1606.014
Niikura H., Takada M., Yokoyama S., Sumi T., Masaki S., 2019, Physical Review D, 99
Paczynski B., 1986, ApJ, 304, 1
Padoan P., Nordlund A., 2002, The Astrophysical Journal, 576, 870–879
Paegert M., Stassun K. G., Collins K. A., Pepper J., Torres G., Jenkins J., Twicken J. D., Latham D. W., 2021, arXiv e-prints, p. arXiv:2108.04778
Payne M. J., Holman M. J., Pál A., 2019, Research Notes of the American Astronomical Society, 3, 172
Pearson S. G., McCaughrean M. J., 2023, arXiv e-prints, p. arXiv:2310.01231
Pont F., Zucker S., Queloz D., 2006, MNRAS, 373, 231

Rasio F. A., Ford E. B., 1996, Science, 274, 954
Ricker G. R., et al., 2015, Journal of Astronomical Telescopes, Instruments, and Systems, 1, 014003
Skrutskie M. F., et al., 2006, AJ, 131, 1163
Smullen R. A., Kratter K. M., Shannon A., 2016, Monthly Notices of the Royal Astronomical Society, 461, 1288–1301
Standing M. R., et al., 2023, Nature Astronomy, 7, 702–714
Strigari L. E., Barnabè M., Marshall P. J., Blandford R. D., 2012, Monthly Notices of the Royal Astronomical Society, 423, 1856–1865
Sumi T., et al., 2023a, The Astronomical Journal, 166, 108
Sumi T., et al., 2023b, AJ, 166, 108
Sutherland A. P., Fabrycky D. C., 2016, The Astrophysical Journal, 818, 6
Veras D., Raymond S. N., 2012, Monthly Notices of the Royal Astronomical Society: Letters, 421, L117–L121
Wang Y., Perna R., Zhu Z., 2024, Floating binary planets from ejections during close stellar encounters (arXiv:2310.06016)
Weidenschilling S. J., Marzari F., 1996, Nature, 384, 619
Welsh W. F., et al., 2011, ApJS, 197, 4
Woods D. F., et al., 2021, PASP, 133, 014503
Wright E. L., et al., 2010, AJ, 140, 1868
Yu F., Lai D., 2024, Free-Floating Planets, Survivor Planets, Captured Planets and Binary Planets from Stellar Flybys (arXiv:2403.07224)
Zacharias N., Finch C. T., Girard T. M., Henden A., Bartlett J. L., Monet D. G., Zacharias M. I., 2013, AJ, 145, 44
Zwart S. P., Hochart E., 2024

This paper has been typeset from a TEX/LATEX file prepared by the author.